

# Ptychographic reconstruction with wavefront initialization

FELIX WITTE<sup>1,2,3</sup> AND PETER MODREGGER<sup>1,2,\*</sup>

<sup>1</sup>Physics Department, University of Siegen, 57072 Siegen, Germany

<sup>2</sup>Center for X-ray and Nano Science CXNS, Deutsches Elektronen-Synchrotron DESY, 22607 Hamburg, Germany

<sup>3</sup>Current address: NERSC, Lawrence Berkeley National Laboratory, Berkeley, California 94720, USA

\*peter.modregger@uni-siegen.de

**Abstract:** X-ray ptychography is a cutting edge imaging technique providing ultra-high spatial resolutions. In ptychography, phase retrieval, i.e., the recovery of a complex valued signal from intensity-only measurements, is enabled by exploiting a redundancy of information contained in diffraction patterns measured with overlapping illuminations. For samples that are considerably larger than the probe we show that during the iteration the bulk information has to propagate from the sample edges to the center. This constitutes an inherent limitation of reconstruction speed for algorithms that use a flat initialization. Here, we experimentally demonstrate that a considerable improvement of computational speed can be achieved by utilizing a low resolution sample wavefront retrieved from measured diffraction patterns as initialization. In addition, we show that this approach avoids phase singularity artifacts due to strong phase gradients. Wavefront initialization is computationally fast and compatible with non-bulky samples. Therefore, the presented approach is readily adaptable with established ptychographic reconstruction algorithms implying a wide spread use.

© 2022 Optica Publishing Group under the terms of the [Optica Publishing Group Publishing Agreement](#)

## Introduction

X-ray ptychography can be regarded as a combination of scanning X-ray transmission microscopy (STXM) and coherent diffraction imaging (CDI). STXM utilizes a lateral scan of the sample through a focused X-ray beam, which provides the transmission function of the specimen [1]. However, spatial resolution is limited by the focus size. CDI, on the other hand, employs an extended X-ray beam larger than the sample and exploits effective oversampling contained in diffraction patterns with additional constraints during algorithmic retrieval [2]. While spatial resolution provided by CDI is at least in principle wavelength limited, the availability of high quality, large X-ray beams practically limit the sample size.

X-ray ptychography integrates the benefits of STXM and CDI by scanning the specimen through a focal spot with overlapping illuminations, which realizes the oversampling required for stable phase retrieval [3–5]. This approach allows for samples that are larger than the focal spot while the achieved spatial resolutions are smaller than the focus size. Data analysis is performed by ptychographic reconstruction algorithms, these are able to retrieve the complex wave field of the sample as well as of the illuminating beam, usually referred to as the probe. Therefore, the quality of ptychographic reconstructions is nearly independent from the quality of the X-ray optics rendering this a lensless technique.

Evidently, the success of ptychographic experiments depend on reliable phase retrieval [6] and, thus, it does not come as a surprise that a wide variety of algorithms have been published. Examples include the extended ptychographic engine (ePIE) [7], 3PIE [8], maximum likelihood refinement [9], scaled gradient ptychography [10], multi-modal ptychography [11] or momentum accelerated ptychography [12]. These algorithms tend to reconstruct the complex wave field associated with the sample (and the probe), whereat the phase is wrapped to values modulus  $2\pi$ .

46 Thus, appropriate phase unwrapping procedures [13, 14] have to be used in order to combine 2D  
47 ptychography with 3D tomography [13, 15, 16]. Refractive ptychography [17, 18], on the other  
48 hand, reconstructs a refractive object function directly and, thus, avoids corresponding phase  
49 wrapping artifacts.

50 These iterative algorithms start with initial guesses for the probe as well as the object and  
51 refine these guesses during the ptychographic reconstruction. Commonly, the probe can be either  
52 directly taken from previous scans or well estimated from experimental parameters. As this is  
53 generally not the case for the object, a flat initialization is generally used for the object's complex  
54 wave field.

55 Here, we show that the STXM information inherent to ptychography measurements can be  
56 exploited to construct a low-resolution estimate of the object's wave field. This estimate is quick  
57 to compute and closely resembles the actual object's wave field. We will demonstrate that using  
58 such an estimate as the initial guess is especially beneficial for bulky samples increasing the  
59 speed of ptychographic iteration while avoiding artifacts associated with large phase gradients.

60 We will first collect elements of the theoretical basis for ptychography and reconstruct the phase  
61 signal of a bulky sample. Thereby, we will demonstrate that the bulk information propagates from  
62 the sample edges to the center during iterative reconstruction. Then, we will describe a procedure  
63 for the retrieval of the sample's complex wave field directly from the measured diffraction patterns.  
64 This low resolution representation of the sample will then be used for wavefront initialization in  
65 ptychographic reconstruction, which improves reconstruction speed and avoid phase artifacts  
66 associated with large phase gradients. Finally, we will show the reconstruction of a worst case  
67 sample (i.e., a non-bulky sample with structures smaller than the probe) is not impaired by  
68 utilizing wavefront initialization.

## 69 Ptychographic reconstruction

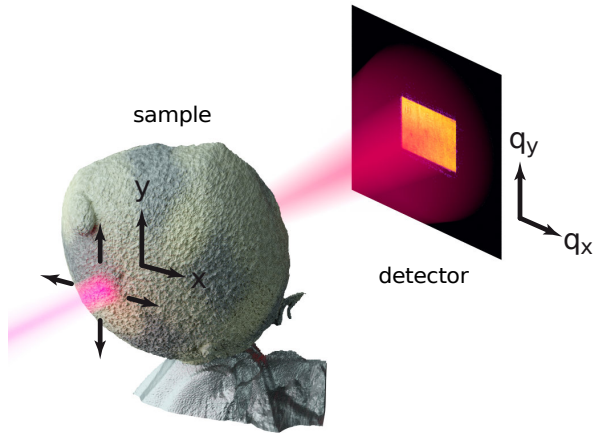


Fig. 1. Sketch of the experimental setup for ptychography.

70 In the following, we will re-iterate elements of the frame work for refractive ptychography [18]  
71 for the convenience of the reader. In the X-ray regime the complex refractive index  $n$  of a material  
72 is commonly expressed as

$$n = 1 - \delta + i\beta, \quad (1)$$

73 with  $\delta$ , the refractive index decrement and  $\beta$ , the absorption index. For samples that are sufficiently  
74 thin to avoid internal diffraction, the complex wave field  $O(\mathbf{r})$  at the object plane point  $\mathbf{r} = (x, y)$

75 (Fig. 1) after transmission is given by

$$O(\mathbf{r}) = \exp(i\tilde{O}(\mathbf{r})) = \exp\left(ik \int dz (n(x, y, z) - 1)\right) \quad (2)$$

76 with  $k$ , the modulus of the wave vector and  $z$ , the direction along the optical axis. The goal of  
77 refractive ptychography is to retrieve the refractive object function  $\tilde{O}(\mathbf{r})$ . In the experiment the  
78 object function is illuminated by a focused X-ray beam with the complex wave field of the probe  
79  $P(\mathbf{r} - \mathbf{R}_j)$  at  $\mathbf{R}_j$  the  $j$ -th scan position. The resulting complex wave field  $\Psi(\mathbf{r})$  is given as

$$\Psi_j(\mathbf{r}) = \exp(i\tilde{O}(\mathbf{r})) \cdot P(\mathbf{r} - \mathbf{R}_j). \quad (3)$$

80 and the observable intensity is

$$\hat{I}_j(\mathbf{q}) = |\mathcal{F}\{\Psi_j(\mathbf{r})\}(\mathbf{q})|^2 \quad (4)$$

81 with  $\mathcal{F}$ , the Fourier transform and  $\mathbf{q} = (q_x, q_y)$  the variables conjugate to  $(x, y)$ . Reconstruction  
82 is achieved by minimizing the cost function  $L$

$$L = \sum_{j, \mathbf{q}} \left| \sqrt{\hat{I}_j(\mathbf{q})} - \sqrt{\hat{D}_j(\mathbf{q})} \right|^2 \quad (5)$$

83 with  $\hat{D}_j(\mathbf{q})$ , the diffraction pattern measured at scan position  $\mathbf{R}_j$ . The use of square roots takes  
84 into account Poisson statistics of photon shot noise [10]. Minimization of  $L$  is usually performed  
85 iteratively for example by the statistical gradient descent scheme [7, 18]. Here, the object wave  
86 field  $O_n(\mathbf{r})$  and the probe wave field  $P_n(\mathbf{r})$  are updated in each iteration step  $n$  as a loop over all  
87 diffraction measurements  $\hat{M}_j(\mathbf{q})$  in a random order. With respect to each diffraction measurement  
88 the update is performed by first calculating the current wave field at the detector

$$\hat{\psi}_j(\mathbf{q}) = \mathcal{F}\{\exp(i\tilde{O}_n(\mathbf{r})) \cdot P_n(\mathbf{r} - \mathbf{R}_j)\}. \quad (6)$$

89 Then the modeled amplitude  $|\hat{\psi}_j(\mathbf{q})|$  is replaced with the amplitude of the measurements  $\sqrt{\hat{D}_j(\mathbf{q})}$   
90 and the resulting wave field is propagated back to the object plane

$$\psi'_j(\mathbf{r}) = \mathcal{F}^{-1}\left\{\sqrt{\hat{D}_j(\mathbf{q})} \cdot \frac{\hat{\psi}_j(\mathbf{q})}{|\hat{\psi}_j(\mathbf{q})|}\right\} \quad (7)$$

91 with  $\mathcal{F}^{-1}$ , the inverse Fourier transform. Finally, the object wave field is updated by

$$\tilde{O}_{n+1}(\mathbf{r}) \leftarrow \tilde{O}_n(\mathbf{r}) + \alpha \frac{(i\psi(\mathbf{r} - \mathbf{R}_j))^*}{\max|\psi(\mathbf{r} - \mathbf{R}_j)|^2} \cdot (\psi'(\mathbf{r}) - \psi(\mathbf{r})) \quad (8)$$

92 and the probe wave field by

$$P_{n+1}(\mathbf{r}) \leftarrow P_n(\mathbf{r}) + \beta \frac{\exp(-i\tilde{O}_n^*(\mathbf{r} + \mathbf{R}_j))}{\max|\exp(-i\tilde{O}_n(\mathbf{r} + \mathbf{R}_j))|^2} \cdot (\psi'(\mathbf{r}) - \psi(\mathbf{r})). \quad (9)$$

93 The update strength is tuned by the parameters  $\alpha$  and  $\beta$ . Initialization of the iterative procedure  
94 refers to the starting values for the object function  $\tilde{O}(\mathbf{r})$  and the probe  $P(\mathbf{r})$ . Usually, a flat  
95 initialization for the object function is chosen, i.e.

$$O_0(\mathbf{r}) = \exp(i\tilde{O}_0(\mathbf{r})) = 1. \quad (10)$$

96 The complex wave field of the probe  $P(\mathbf{r})$  is usually well characterized, which allows a realistic  
97 initialization.

98 For the experimental demonstration of our proposed approach we will reuse a previously  
99 published ptychographic scan of a micrometeorite [18]. The essential experimental parameters  
100 were as follows. The scan was carried out at the P06 beamline of PETRA III (DESY, Hamburg) [19,  
101 20] using the combined Micro- and Nanoprobe setup [21]. The X-ray beam with a photon  
102 energy of 18 keV was focused by two orthogonal Kirkpatrick–Baez mirrors to a probe size of  
103  $300 \text{ nm} \times 200 \text{ nm}$  at the position of the sample. The micrometeorite with a diameter of about  
104  $80 \text{ }\mu\text{m}$  was scanned in fly-mode over a field of view of  $100 \text{ }\mu\text{m} \times 100 \text{ }\mu\text{m}$  in steps of 200 nm  
105 resulting in 250,000 scan points. The diffraction patterns were recorded with an EIGER 500k  
106 (Dectris, Switzerland) located 8.75 m downstream of the sample with a dwell time of 1 ms. The  
107 central  $128 \times 128$  pixels were used for ptychographic reconstruction yielding a effective pixel  
108 size of 62.8 nm. Iterative reconstruction was performed based on refractive ptychography as  
109 described above and by scaled gradient descent [10] with an additional momentum accelerated  
110 update [12] every second iteration step.

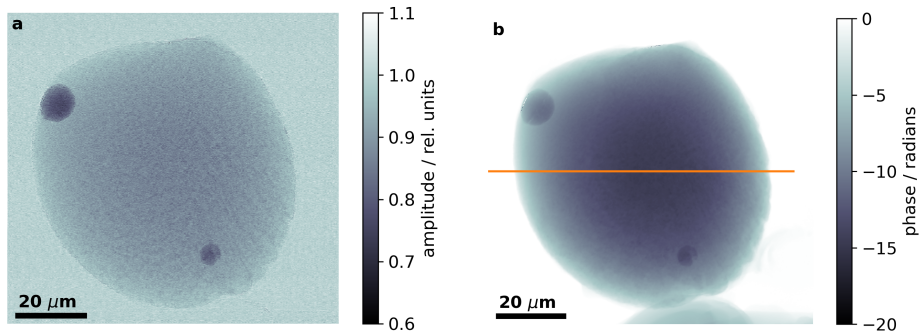


Fig. 2. Modulus (a) and phase (b) of the micrometeorite as retrieved by refractive ptychography. The field of view is  $100 \text{ }\mu\text{m} \times 100 \text{ }\mu\text{m}$ . The horizontal line in (b) indicates the position of the lines profiles in Fig. 3.

111 Figure 2 shows the result of refractive ptychographic reconstruction with flat initialization  
112 (eq. 10). Artifacts at the left and the top edges of the sample appear in the reconstruction of the  
113 phase, which can be attributed to large phase gradients (see below). Clearly, the micrometeorite  
114 constitutes a bulky sample, which is about 400 times larger than the probe.

115 Figure 3 illustrates the behaviour of the reconstructed phase signal as a function of iteration  
116 steps for this bulky sample. It is evident that during iteration the bulk information propagates  
117 from the edges of the sample to the center, which can be explained as follows. Phase information  
118 is predominately encoded in the lateral offset of the diffraction patterns due to refraction or,  
119 equivalently, phase gradients. Thus, there is little difference between the exterior of the sample  
120 and its center as the phase gradients in both regions are negligible. Therefore, bulk phase information  
121 is most prevalent only at the edges of the sample. In each iteration step this information can only  
122 be shared between neighboring scan points, which leads to a large number of required iteration  
123 steps for bulky samples. Initialising the ptychographic reconstruction with a sample wave field  
124 that already carries bulk information can improve reconstruction speed considerably in contrast  
125 to a flat initialization.

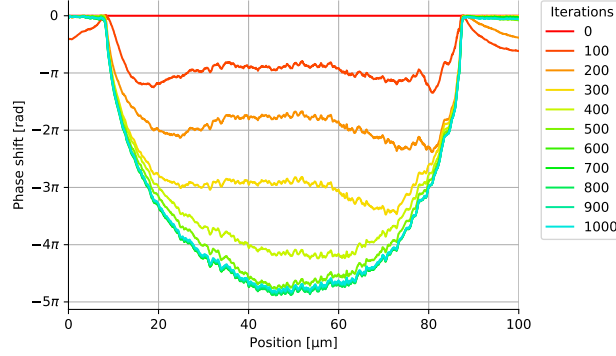


Fig. 3. Horizontal line profiles (Fig. 2b) of the reconstructed phase signal through the middle of the micrometeorite as a function of iteration steps. With each iteration, the reconstructed phase improves from the edges of the sample towards the center.

## 126 Moment analysis

127 The sample's complex wavefront  $O(\mathbf{R}_j) = o(\mathbf{R}_j)e^{i\Phi(\mathbf{R}_j)}$  with the object's transmission  $o(\mathbf{R}_j)$   
 128 and the object's phase  $\Phi(\mathbf{R}_j)$  will be constructed from the moments  $M_{uv}$  of the measured  
 129 diffraction patterns  $\hat{D}_j(\mathbf{q})$ , which are given as [22–24]

$$M_{uv}(\mathbf{R}_j) = \int d\mathbf{q} (q_x)^u (q_y)^v \hat{D}_j(\mathbf{q}) \quad (11)$$

130 with  $u$  and  $v$  both integers indicating the horizontal and vertical order of the moment, respectively.  
 131 In the following, we will be only interested in the three moments up to the first order. The  
 132 transmission signal of the object corresponds to  $M_{00}$  in a straight forward way:

$$o^2(\mathbf{R}_j) = \frac{\int d\mathbf{q} \hat{D}_j(\mathbf{q})}{\int d\mathbf{q} \hat{D}_{\text{flat}}(\mathbf{q})} \quad (12)$$

133 with  $D_{\text{flat}}(\mathbf{q})$  a diffraction pattern taken in a region outside the object for the purpose of  
 134 normalization.

135 Typically, the horizontal differential phase signal of the object  $\Phi_x(\mathbf{R}_j) = \partial_x \Phi(\mathbf{R}_j)$  is associated  
 136 with  $M_{10}$  and the vertical differential phase signal  $\Phi_y(\mathbf{R}_j) = \partial_y \Phi(\mathbf{R}_j)$  with  $M_{01}$ . However, this  
 137 association relies on at least two implicit assumptions as demonstrated in [22] and which we will  
 138 show in the following. It has been analytically demonstrated that the moments of the diffraction  
 139 patterns  $M_{uv}$  are connected to the complex input wavefield in direct space  $\Psi(\mathbf{r})$  by a simple  
 140 integral [25]. For  $M_{10}$  this is given as

$$M_{10}(\mathbf{R}_j) = \frac{1}{-iK} \int d\mathbf{r} \Psi_j^*(\mathbf{r}) \partial_x \Psi_j(\mathbf{r}) \quad (13)$$

141 with the modulus of the wave vector  $K$  and an analogous equation for  $M_{01}$ , which involves  
 142 the partial derivative  $\partial_y$ . Using eq. (3) and  $P(\mathbf{r} - \mathbf{R}_j) = p(\mathbf{r} - \mathbf{R}_j)e^{i\xi(\mathbf{r} - \mathbf{R}_j)}$  with the probe's  
 143 transmission  $p(\mathbf{r} - \mathbf{R}_j)$  and the probe's phase  $\xi(\mathbf{r} - \mathbf{R}_j)$  leads to

$$M_{10}(\mathbf{R}_j) = \int d\mathbf{r} [p^2(\mathbf{r} - \mathbf{R}_j)o^2(\mathbf{r}) \partial_x \Phi(\mathbf{r}) + p^2(\mathbf{r} - \mathbf{R}_j)o^2(\mathbf{r}) \partial_x \xi(\mathbf{r})], \quad (14)$$

144 where terms involving derivatives of the transmission signals vanish, since the probe has a finite  
 145 support:  $\int d\mathbf{r} p(\mathbf{r}) \partial_x p(\mathbf{r}) = p^2(\mathbf{r})/2|_{-\infty}^{\infty} = 0$ . The first term in eq. (14) corresponds to the

146 object's phase gradient, which is of interest here. The second term constitutes a contribution of  
 147 the probe to  $M_{10}$  and is non-zero in the combined case of a non-vanishing absorption signal of the  
 148 object  $o(\mathbf{R}_j) \neq 1$  and a non-vanishing phase gradient of the probe  $\partial_x \xi(\mathbf{r} - \mathbf{R}_j) \neq 0$ . The latter is  
 149 typically the case if the object is located outside of the beam focus, the optics are aberrated, or if  
 150 a purposefully structured probe is used.

151 Assuming that the second term in eq. (14) can be neglected, the differential phase signals of  
 152 the object in the area of illumination defined by the probe  $P(\mathbf{r} - \mathbf{R}_j)$  at the scan point  $\mathbf{R}_j$  can be  
 153 estimated as

$$\Phi_x(\mathbf{R}_j) = \frac{\int d\mathbf{q} q_x \hat{D}_j(\mathbf{q})}{\int d\mathbf{q} \hat{D}_j(\mathbf{q})} - \frac{\int d\mathbf{q} q_x \hat{D}_{\text{flat}}(\mathbf{q})}{\int d\mathbf{q} \hat{D}_{\text{flat}}(\mathbf{q})} \quad (15)$$

154 and

$$\Phi_y(\mathbf{R}_j) = \frac{\int d\mathbf{q} q_y \hat{D}_j(\mathbf{q})}{\int d\mathbf{q} \hat{D}_j(\mathbf{q})} - \frac{\int d\mathbf{q} q_y \hat{D}_{\text{flat}}(\mathbf{q})}{\int d\mathbf{q} \hat{D}_{\text{flat}}(\mathbf{q})}, \quad (16)$$

155 where correction terms account for the pixel position of the flat field beam in the detector.

156 If the second term in eq. (14) cannot be neglected, the above equations have to be corrected.  
 157 For this, the influence of the object's transmission and the probe's differential phase signal must  
 158 be determined. This can be done by either using the second term directly or – more conveniently  
 159 – by calculating virtual diffraction patterns  $\hat{V}_j(\mathbf{q})$  provided by the pure absorption signal of the  
 160 object according to

$$\hat{V}_j(\mathbf{q}) = |\mathcal{F}\{o(\mathbf{R}_j)P(\mathbf{r} - \mathbf{R}_j)\}(\mathbf{q})|^2. \quad (17)$$

161 The moments  $M_{10}$  and  $M_{01}$  of these virtual diffraction pattern correspond exactly to the second  
 162 term in eq. (14). Thus, the differential phase signals can be estimated in this case as

$$\Phi_x(\mathbf{R}_j) = \frac{\int d\mathbf{q} q_x \hat{D}_j(\mathbf{q})}{\int d\mathbf{q} \hat{D}_j(\mathbf{q})} - \frac{\int d\mathbf{q} q_x \hat{V}_j(\mathbf{q})}{\int d\mathbf{q} \hat{V}_j(\mathbf{q})} \quad (18)$$

163 and

$$\Phi_y(\mathbf{R}_j) = \frac{\int d\mathbf{q} q_y \hat{D}_j(\mathbf{q})}{\int d\mathbf{q} \hat{D}_j(\mathbf{q})} - \frac{\int d\mathbf{q} q_y \hat{V}_j(\mathbf{q})}{\int d\mathbf{q} \hat{V}_j(\mathbf{q})}. \quad (19)$$

## 164 Wavefront retrieval

165 In order to retrieve the phase image  $\Phi(\mathbf{R}_j)$  from the estimated differential phase images  $\Phi_x(\mathbf{R}_j)$   
 166 and  $\Phi_y(\mathbf{R}_j)$  we use the non-iterative, boundary-artifact-free wavefront reconstruction presented  
 167 in [26]. This approach starts with constructing an antisymmetric extension of the inputs

$$\bar{\Phi}_x = \begin{bmatrix} -\Phi_x(-x, -y) & \Phi_x(x, -y) \\ -\Phi_x(-x, y) & \Phi_x(x, y) \end{bmatrix} \quad (20)$$

168 and

$$\bar{\Phi}_y = \begin{bmatrix} -\Phi_y(-x, -y) & -\Phi_y(x, -y) \\ \Phi_y(-x, y) & \Phi_y(x, y) \end{bmatrix}. \quad (21)$$

169 Then the integrated image is retrieved by calculating

$$\bar{\Phi}(\mathbf{R}_j) = \mathcal{F}^{-1} \left\{ \frac{\mathcal{F}\{\bar{\Phi}_x\}(\mathbf{q}) + i\mathcal{F}\{\bar{\Phi}_y\}(\mathbf{q})}{q_x + iq_y} \right\}, \quad (22)$$

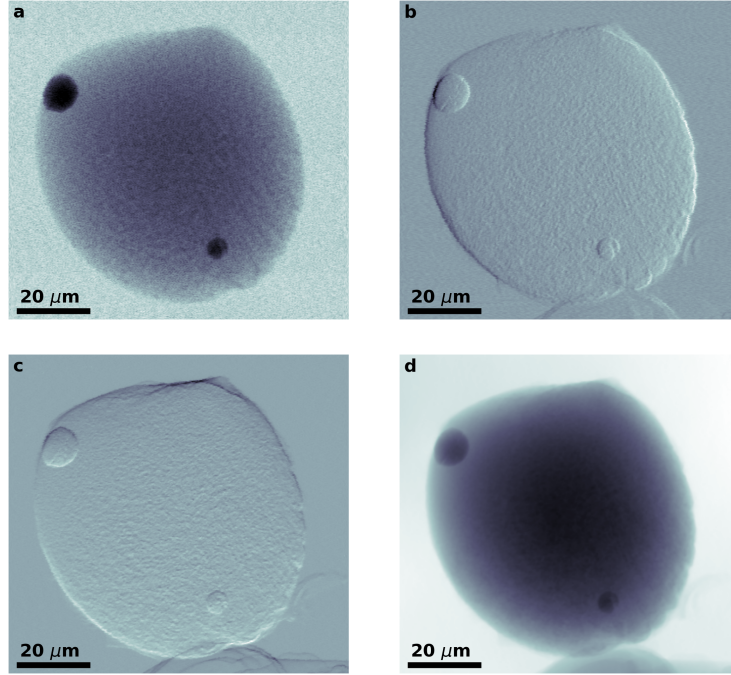


Fig. 4. Non-iterative wavefront retrieval of the sample's complex wave field used for subsequent initialization. The moment analysis of diffraction patterns provide the absorption (a), horizontal (b) and vertical phase gradients (c). The combination of the absorption image (a) and the non-iteratively retrieved phase (d) provide a complex wave field of the sample with low spatial resolution.

170 which was also published in [27]. Final cropping of  $\bar{\Phi}(\mathbf{R}_j)$  to the region of interest yields a  
 171 low resolution representation of the object phase  $\Phi(\mathbf{R}_j)$ . The results of non-iterative wavefront  
 172 retrieval for the micrometeorite sample are illustrated in Fig. 4. Here, the phase gradient of the  
 173 probe was negligible, so that eqs. (15) and (16) have been used for the estimation of the phase  
 174 gradients.

### 175 Ptychographic reconstruction with wavefront retrieval

176 With the availability of the low resolution versions of the absorption and the phase image the  
 177 initialization for the sample's complex wave field is given by

$$O_0(\mathbf{r}) = o(\mathbf{R}_j) \cdot \exp(i\Phi(\mathbf{R}_j)), \quad (23)$$

178 where interpolation between the coordinate systems defined by  $\mathbf{r}$  and  $\mathbf{R}_j$  is used as necessary.

179 Figure 5 shows the resulting phase signal of the micrometeorite after 1000 iteration steps for  
 180 flat initialization in panel (a) and wavefront initialization in panel (b). As expected the images  
 181 are fairly similar. However, in the reconstruction with flat initialization (a) phase singularities  
 182 are present at the left and the top border of the sample coinciding with the locations of the  
 183 largest phase gradients visible in Fig. 4 (b) and (c). These artifacts are absent for ptychographic  
 184 reconstruction with wavefront initialization (insets in Fig. 5b).

185 In order to demonstrate the versatility of the wavefront initialization for ptychographic  
 186 reconstructions, the proposed approach was further applied to a ptychographic data set which was

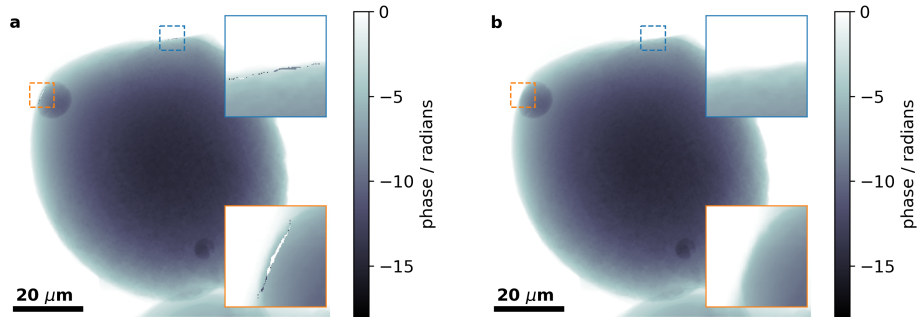


Fig. 5. The retrieved phase signals of the micrometeorite with flat initialization (a) and wavefront initialization (b) are broadly similar as expected. The insets show magnified regions, where phase singularities occur with flat initialization and are located at positions of the largest phase gradients (cmp. to Fig. 4 b and c). These artifacts are avoided by using wavefront initialization as shown by the inset in (b).

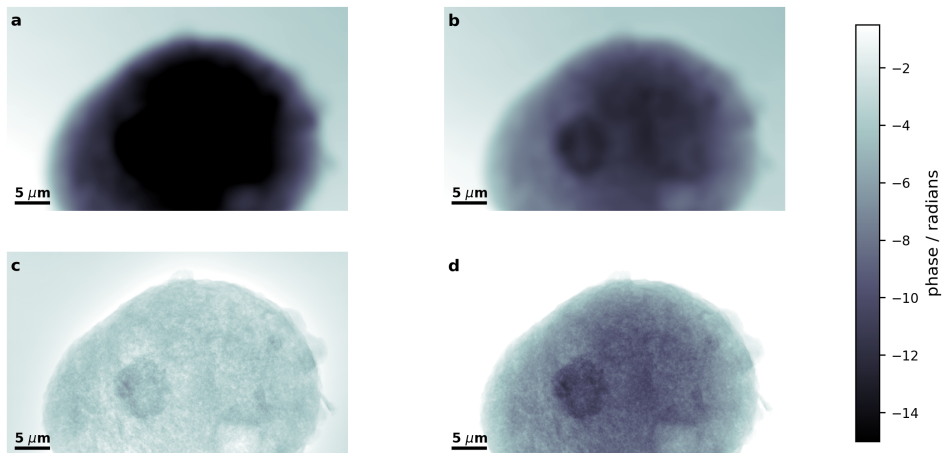


Fig. 6. Estimated phase and ptychographic reconstruction of a fluid catalytic cracking catalyst particle. (a) Estimated phase without the necessary correction for the probe influence (i.e., using eqs. 15 and 16). (b) Estimated phase with the necessary correction for the probe influence (i.e., using eqs. 18 and 19). (c) Ptychographic reconstruction of the object's phase signal with flat initialization. (d) Ptychographic reconstruction of the object's phase signal with wave front initialization. The data set was taken from [28].



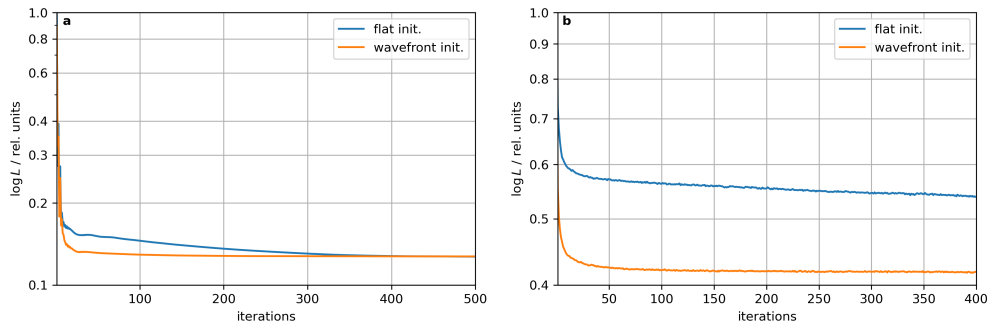


Fig. 7. Comparison of the logarithmic value of the cost function  $L$  (eq. 5) between flat and wavefront initialization as a function of iteration steps for (a) the micrometeorite data and (b) the fluid catalytic cracking catalyst particle. Ptychographic reconstruction with wavefront initialization converges about 200 iteration steps faster in case of (a) and provides superior convergence over the course of 400 iterations in case of (b).

187 acquired at the cSAXS beamline of the Swiss Light Source, PSI, Switzerland [29]. Here a fluid  
 188 catalytic cracking catalyst particle with a diameter of  $20\ \mu\text{m}$  was scanned with a photon energy  
 189 of 6.2 keV over 2344 positions in a spiral trajectory. The average step size was  $0.8\ \mu\text{m}$  covering a  
 190 field of view of  $50\ \mu$  by  $30\ \mu$ . The pixel size of the reconstruction was 29 nm. More details of  
 191 the setup and scan procedure can be found in the original work [30] and the data set is available  
 192 online [28]. One of the goals of Odrščil *et al* was to show that purposefully structured probes  
 193 can improve ptychographic reconstructions. However, the data set used in the following (named  
 194 "FCC\_particle\_FZP\_11\_dataset\_id1.mat") was acquired without a structured probe, but since  
 195 the object was placed out of the beam focus, the probe still showed a noticeable phase gradient.

196 Figure 6 summarizes the results of ptychographic reconstruction of this data set in the context  
 197 at hand. Panel (a) shows the estimation of the object's phase without appropriate correction for  
 198 the probe's phase gradient (i.e., using eqs. (15) and (16)). Apparently, the object's phase shift was  
 199 significantly overestimated. Panel (b) demonstrates that the appropriate correction (i.e., using  
 200 eqs. (18) and (19)) solves this issue. Panel (c) displays the result of refractive ptychographic  
 201 reconstruction and flat initialization after 400 iteration steps (equivalent to Fig. 5a in [30]). Panel  
 202 (d) shows the result of ptychographic reconstruction with wavefront initialization, i.e. the phase  
 203 estimation in panel (b) plus the corresponding absorption signal was used to initialize the iterative  
 204 minimization. Remarkably, this result is equivalent to Fig. 5d in [30] without using a structured  
 205 probe. This has potential benefits for combining ptychography with other X-ray techniques that  
 206 would suffer from structured probes, such as X-ray fluorescence.

207 Using wavefront initialization (eq. 23) implies that the bulk phase information associated  
 208 with the sample is already present and iteration steps that are associated with the propagation  
 209 of information from the edges to the center of the sample are skipped during ptychographic  
 210 reconstruction. Figure 7 demonstrates that this saves several hundred iteration steps in case of the  
 211 micrometeorite or even provides superior convergence over the first 400 iteration steps in case  
 212 of the fluid catalytic cracking catalyst particle. Therefore, ptychographic reconstruction with  
 213 wavefront initialization can improve iteration speed considerably.

214 Up to now, the samples included in this study were considerably bulky and, thus, well suited to  
 215 benefit from ptychographic reconstruction with wavefront initialization. In order to investigate  
 216 the performance for samples that are more challenging in the present context, we have used  
 217 numerical simulations of a Siemensstar pattern. In this case, the sample is flat with structures  
 218 smaller than the probe and, thus, there is no bulk information to propagate during iteration.

219 The simulated Siemensstar was sampled on a  $213 \times 213$  grid and provided a minimum

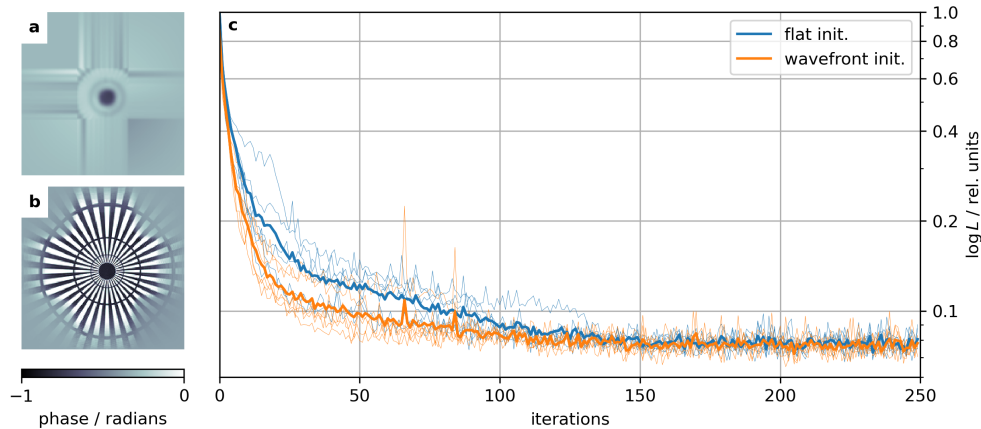


Fig. 8. Ptychographic reconstruction of a Siemens star with numerical simulations. (a) Low-resolution phase estimate. (b) Retrieved phase distribution using wavefront initialization. (c) Comparison of the logarithmic value of the cost function  $L$  (eq. 5) between flat and wavefront initialization as a function of iteration steps. Thick lines are the average values of the cost function of 6 repeated reconstructions (thin lines). While wavefront initialization performs better than flat initialization in the beginning, both take about the same number of iteration steps to converge.

220 transmission of 0.8 and a phase shift of -1.2 rad (Fig. 8b), which corresponds to Au structures  
 221 with a height of 650 nm imaged at a photon energy of 8.2 keV. The probe had a Gaussian-like  
 222 shape with a full width half maximum of 7 pixels, which is markedly larger than the smallest  
 223 sample features. The observable diffraction patterns were calculated according to eq. (4) and  
 224 wavefront retrieval was performed as described above.

225 Although the estimated wave field for the object used for initialization has insufficient resolution  
 226 to sample the Siemenstar (Fig. 8a), the reconstructed object's phase distribution (Fig. 8b) shows  
 227 that structures smaller than the probe are still reliably retrieved using wavefront initialization.  
 228 This demonstrates that wavefront initialization is compatible even with challenging samples.  
 229 However, the comparison of the cost function  $L$  between flat and wavefront initialization (Fig. 8c)  
 230 illustrates only a negligible difference in terms of convergence speed.

## 231 Conclusion

232 We have demonstrated that the speed of ptychographic reconstruction algorithms which use a flat  
 233 initialization for the sample's complex wave field is inherently limited for bulky samples. This is  
 234 due to the fact that during the iterations the bulk phase information has to propagate from the  
 235 edges of the sample to its center. By instead using wavefront initialization, the reconstruction  
 236 speed is considerably increased as the bulk phase information is already present. In addition, we  
 237 have shown that wavefront initialization can avoid phase singularity artifacts associated with  
 238 large phase gradients.

239 The input data for constructing the wavefront initialization is readily accessible in most  
 240 ptychographic scans via moment analysis of the measured diffraction patterns. The corresponding  
 241 algorithm for retrieving the complex wave field is – compared to the ptychographic reconstruction –  
 242 fast. In addition, wavefront initialization is readily compatible with a broad range of ptychographic  
 243 reconstruction algorithms. Taken all together, this makes the presented approach attractive for  
 244 most ptychography applications.

## 245 Acknowledgements

246 We acknowledge DESY (Hamburg, Germany), a member of the Helmholtz Association HGF, for  
247 the provision of experimental facilities. Parts of this research was carried out at the PETRA III  
248 beamline P06. We thank Dennis Brückner, Stijen van Malderen and Jan Garrevoet for assistance  
249 in using P06. This research was supported in part through the Maxwell computational resources  
250 operated at Deutsches Elektronen-Synchrotron DESY, Hamburg, Germany.

## 251 References

- 252 1. A. Sakdinawat and D. Attwood, "Nanoscale X-ray imaging," *Nat. Photonics* **4**, 840–848 (2010).
- 253 2. H. N. Chapman and K. A. Nugent, "Coherent lensless X-ray imaging," *Nat. Photonics* **4**, 833–839 (2010).
- 254 3. H. M. Faulkner and J. M. Rodenburg, "Movable aperture lensless transmission microscopy: A novel phase retrieval  
255 algorithm," *Phys. Rev. Lett.* **93**, 2–5 (2004).
- 256 4. P. Thibault, M. Dierolf, A. Menzel, O. Bunk, C. David, and F. Pfeiffer, "High-resolution scanning X-ray diffraction  
257 microscopy," *Sci. (80-. )*. **321**, 379–382 (2008).
- 258 5. F. Pfeiffer, "X-ray ptychography," *Nat. Photonics* **12**, 9–17 (2018).
- 259 6. Y. Shechtman, Y. C. Eldar, O. Cohen, H. N. Chapman, J. Miao, and M. Segev, "Phase Retrieval with Application to  
260 Optical Imaging," *IEEE Signal Process. Mag.* **32**, 87–109 (2014).
- 261 7. A. M. Maiden and J. M. Rodenburg, "An improved ptychographical phase retrieval algorithm for diffractive imaging,"  
262 *Ultramicroscopy* **109**, 1256–1262 (2009).
- 263 8. A. M. Maiden, M. J. Humphry, and J. M. Rodenburg, "Ptychographic transmission microscopy in three dimensions  
264 using a multi-slice approach," *J. Opt. Soc. Am. A* **29**, 1606 (2012).
- 265 9. P. Thibault and M. Guizar-Sicairos, "Maximum-likelihood refinement for coherent diffractive imaging," *New J. Phys.*  
266 **14** (2012).
- 267 10. P. Godard, M. Allain, V. Chamard, and J. Rodenburg, "Noise models for low counting rate coherent diffraction  
268 imaging," *Opt. Express* **20**, 25914 (2012).
- 269 11. P. Thibault and A. Menzel, "Reconstructing state mixtures from diffraction measurements," *Nature* **494**, 68–71  
270 (2013).
- 271 12. A. Maiden, D. Johnson, and P. Li, "Further improvements to the ptychographical iterative engine," *Optica* **4**, 736  
272 (2017).
- 273 13. M. Guizar-Sicairos, A. Diaz, M. Holler, M. S. Lucas, A. Menzel, R. A. Wepf, and O. Bunk, "Phase tomography from  
274 x-ray coherent diffractive imaging projections," *Opt. Express* **19**, 21345 (2011).
- 275 14. M. Stockmar, I. Zanette, M. Dierolf, B. Enders, R. Clare, F. Pfeiffer, P. Cloetens, A. Bonnin, and P. Thibault, "X-ray  
276 near-field ptychography for optically thick specimens," *Phys. Rev. Appl.* **3**, 1–6 (2015).
- 277 15. M. Dierolf, A. Menzel, P. Thibault, P. Schneider, C. M. Kewish, R. Wepf, O. Bunk, and F. Pfeiffer, "Ptychographic  
278 X-ray computed tomography at the nanoscale," *Nature* **467**, 436–439 (2010).
- 279 16. A. Diaz, P. Trtik, M. Guizar-Sicairos, A. Menzel, P. Thibault, and O. Bunk, "Quantitative x-ray phase nanotomography,"  
280 *Phys. Rev. B - Condens. Matter Mater. Phys.* **85**, 1–4 (2012).
- 281 17. S. Chowdhury, M. Chen, R. Eckert, D. Ren, F. Wu, N. Repina, and L. Waller, "High-resolution 3D refractive index  
282 microscopy of multiple-scattering samples from intensity images," *Optica* **6**, 1211 (2019).
- 283 18. F. Wittwer, J. Hagemann, D. Brückner, S. Flenner, and C. G. Schroer, "Phase retrieval framework for direct  
284 reconstruction of the projected refractive index applied to ptychography and holography," *Optica* **9**, 295 (2022).
- 285 19. C. G. Schroer, M. Seyrich, M. Kahnt, S. Botta, R. Döhrmann, G. Falkenberg, J. Garrevoet, M. Lyubomirskiy,  
286 M. Scholz, A. Schropp, and F. Wittwer, "PtyNAMi: Ptychographic Nano-Analytical Microscope at PETRA III:  
287 interferometrically tracking positions for 3D x-ray scanning microscopy using a ball-lens retroreflector," in *SPIE Opt.*  
288 *Eng. + Appl.*, (2017), September 2017, p. 13.
- 289 20. A. Schropp, R. Dohrmann, S. Botta, D. Bruckner, M. Kahnt, M. Lyubomirskiy, C. Ossig, M. Scholz, M. Seyrich,  
290 M. E. Stuckelberger, P. Wiljes, F. Wittwer, J. Garrevoet, G. Falkenberg, Y. Fam, T. L. Sheppard, J. D. Grunwaldtd,  
291 and C. G. Schroer, "PtyNAMi: Ptychographic nano-analytical microscope," *J. Appl. Crystallogr.* **53**, 957–971 (2020).
- 292 21. A. Schropp, D. Brückner, J. Bulda, G. Falkenberg, J. Garrevoet, J. Hagemann, F. Seiboth, K. Spiers, F. Koch,  
293 C. David, M. Gambino, M. Veselý, F. Meirer, and C. G. Schroer, "Full-field hard X-ray microscopy based on  
294 aberration-corrected Be CRLs," in *Proc. SPIE 11112*, vol. 1111208 (2019), p. 7.
- 295 22. P. Thibault, M. Dierolf, C. M. Kewish, A. Menzel, O. Bunk, and F. Pfeiffer, "Contrast mechanisms in scanning  
296 transmission x-ray microscopy," *Phys. Rev. A - At. Mol. Opt. Phys.* **80** (2009).
- 297 23. O. Bunk, M. Bech, T. H. Jensen, R. Feidenhansl, T. Binderup, A. Menzel, and F. Pfeiffer, "Multimodal x-ray scatter  
298 imaging," *New J. Phys.* **11** (2009).
- 299 24. P. Modregger, S. Rutishauser, J. Meiser, C. David, and M. Stampanoni, "Two-dimensional ultra-small angle X-ray  
300 scattering with grating interferometry," *Appl. Phys. Lett.* **105** (2014).
- 301 25. P. Modregger, M. Kagias, S. C. Irvine, R. Brönnimann, K. Jefimovs, M. Endrizzi, and A. Olivo, "Interpretation and  
302 utility of the moments of small-angle x-ray scattering distributions," *Phys. Rev. Lett.* **118**, 265501 (2017).
- 303 26. P. Bon, S. Monneret, and B. Wattellier, "Noniterative boundary-artifact-free wavefront reconstruction from its  
304 derivatives," *Appl. Opt.* **51**, 5698–5704 (2012).

- 305 27. C. Kottler, C. David, F. Pfeiffer, and O. Bunk, "A two-directional approach for grating based differential phase  
306 contrast imaging using hard x-rays," *Opt. Express* **15**, 1175 (2007).
- 307 28. M. Odstrčil and M. Holler, "X-ray dataset for illumination improvements for high-resolution ptychography,  
308 <http://dx.doi.org/10.5281/zenodo.2639759>," (2019).
- 309 29. M. Holler, A. Diaz, M. Guizar-Sicairos, P. Karvinen, E. Färm, E. Härkönen, M. Ritala, A. Menzel, J. Raabe, and  
310 O. Bunk, "X-ray ptychographic computed tomography at 16 nm isotropic 3D resolution," *Sci. Rep.* **4**, 1–5 (2014).
- 311 30. M. Odstrčil, M. Lebugle, M. Guizar-Sicairos, C. David, and M. Holler, "Towards optimized illumination for  
312 high-resolution ptychography," *Opt. Express* **27**, 14981 (2019).